

# Extending the Dynamic Range of Electronics in a Time Projection Chamber

J. Estee<sup>a,b</sup>, W.G. Lynch<sup>a,b</sup>, J. Barney<sup>a,b</sup>, G. Cerizza<sup>a,b</sup>, B. Hong<sup>c</sup>, T. Isobe<sup>d</sup>,  
G. Jhang<sup>a</sup>, M. Kaneko<sup>e</sup>, M. Kurata-Nishimura<sup>d</sup>, P. Lasko<sup>f</sup>, J. W. Lee<sup>c</sup>, J.  
Łukasik<sup>f</sup>, A.B. McIntosh<sup>g</sup>, T. Murakami<sup>e</sup>, P. Pawłowski<sup>f</sup>, K. Pelczar<sup>i</sup>, C.  
Santamaria<sup>a</sup>, D. Suzuki<sup>d</sup>, M. B. Tsang<sup>a</sup>, R. Wang<sup>j,k</sup>, S.J. Yennello<sup>g</sup>, Y.  
Zhang<sup>h</sup>, and the S $\pi$ RIT collaboration

<sup>a</sup>National Superconducting Cyclotron Laboratory, East Lansing, Michigan, 48824, USA

<sup>b</sup>Department of Physics and Astronomy, Michigan State University, East Lansing,  
Michigan, 48824, USA

<sup>c</sup>Department of Physics, Korea University, Seoul 136-703, Republic of Korea

<sup>d</sup>RIKEN Nishina Center, Hirosawa 2-1, Wako, Saitama 351-0198, Japan

<sup>e</sup>Department of Physics, Kyoto University, Kita-shirakawa, Kyoto 606-8502, Japan

<sup>f</sup>Institute of Nuclear Physics PAN, ul. Radzikowskiego 15231-342 Kraków, Poland

<sup>g</sup>Cyclotron Institute, Texas A&M University, College Station, TX 77843, USA

<sup>h</sup>Department of Physics, Tsinghua University, Beijing 100084, P. R. China

<sup>i</sup>Faculty of Physics, Astronomy and Applied Computer Science, Jagiellonian University, ul.  
Gołębia 24, 31-007 Kraków

<sup>j</sup>State Key Laboratory of Radiation Medicine and Protection, School of Radiation Medicine  
and Protection, Soochow University, Suzhou 215123, China

<sup>k</sup>Collaborative Innovation Center of Radiological Medicine of Jiangsu Higher Education  
Institutions, Suzhou 215123, China

---

## Abstract

When Time Projection Chambers (TPCs) are used in low to intermediate heavy ion collisions, the mass and momentum range covered by the emitted particles cover a wide range in energy losses. Many TPC readout electronics currently only have a single gain output with a fixed dynamic range. In a recent set of experiments using the SAMURAI Pion-Reconstruction and Ion-Tracker (S $\pi$ RIT) TPC, it was important to simultaneously measure relativistic pions and heavy ion tracks from the same collisions. As a tracks energy loss is collected and multiplied by the anode wires, a distribution of image charges are induced on the TPC read out pads. If the avalanche on a wire is large enough, the charge collected on a pad will saturate the electronics, though only for pads directly underneath the avalanche; pads further away in the distribution will not be saturated. Using these unsaturated pads and the known distribution

function, we can estimate the saturated pads, increasing the dynamic range by a factor of 5.

*Keywords:* `elsarticle.cls`, L<sup>A</sup>T<sub>E</sub>X, Elsevier, template

*2010 MSC:* 00-01, 99-00

---

## 1. Introduction

As charged particles resulting from a heavy ion collision (HIC) pass through a Time Projection Chamber (TPC), they ionize the gas inside of the drift region of the chamber. These electrons drift under influence of the electric and magnetic fields in the to the avalanche region where they are multiplied in the presence of the high electric fields of wire, GEM, or Mircromega structures. Image currents induced in nearby pad electrodes are read out into electronics to obtain the trajectories and stopping powers,  $\langle dE/dx \rangle$ , of the charged particles traversing the TPC.

In high energy HIC, most of these particles have charges of  $\pm e$  and stopping powers which span a relatively narrow range; the dynamical range of TPC readout electronics typically reflects this narrow range of stopping powers. Challenges emerge when applying TPCs to low or intermediate energy HIC where stopping powers range from the very small values for minimum ionizing particles to the much higher stopping powers of slower moving, heavy fragments.

Figure 1 shows some of the stopping powers of light particles with  $Z=1-3$  typically measured in  $^{132}\text{Sn} + ^{124}\text{Sn}$  collisions at an intermediate incident energy of  $E/A=270$  MeV by the SAMURAI Pion Reconstruction and Ion-Tracker ( $S\pi RIT$ ) TPC, [1]. Here the red lines in the figure are the predicted energy loss, the most probable  $dE/dx$ , as a function of rigidity  $P/q$ , generated from Geant4 simulations.

The dynamic range expected from TPC electronics is on the order of 1000:1 signal to noise ratio for the maximum signal. The position measurement of a track comes from fitting the induced charge distribution on several pads. As an example the middle pad has the largest signal the small pads adjacent to it need

to have at least a signal to noise ratio of 6:1. If they hold 10% of the charge each then the largest signal, holding 80% of the charge, has a signal to noise of around 50:1.

Therefore the maximum signal in a TPC is roughly 20 times that of a minimum ionizing particle's signal. The blue dashed lines in Figure 1, located at the top and bottom of the vertical blue bar, are separated by a factor of 20, representing the typical effective dynamic range in a TPC.

This dynamic range estimate should be regarded as approximate because the energy loss fluctuates significantly from the mean value predicted from the most probable energy loss as described in Bichsel [2]. Nevertheless, the blue dashed lines and vertical blue bar illustrate the range of energy losses that any fixed gain readout system can sample is limited; one can change the gain and shift the energy loss range that can be sampled, but not increase the range of it.

The hyperbolic increase in the stopping powers at low momentum illustrates the degree to which the range of stopping powers can exceed the electronics effective dynamic range and highlights the problems encountered in studies of intermediate energy collisions, in which light particles are abundantly produced with low momenta and more highly charged particles are emitted as well. Similar problems are encountered when TPCs are used as active targets in direct reaction studies with rare isotope beams [3] [CITE ANOTHER ARTICLE??? BILL???].

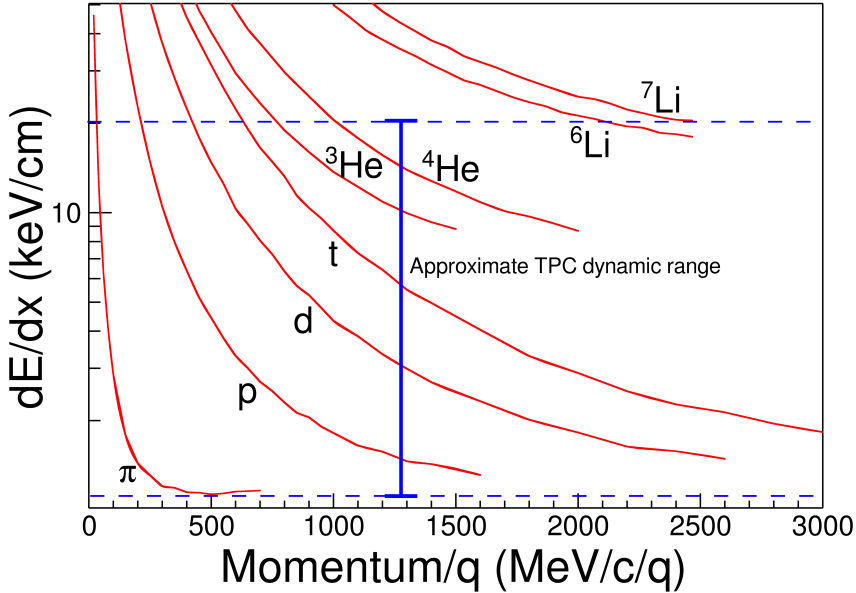


Figure 1: The expected  $dE/dx$  lines of different particles are given in red as calculated by GEANT4. The approximate dynamic range of the TPC is shown for the gain setting used in the experiment. Anything outside of this region would be saturated to some degree.

Several techniques have been employed to increase the range in energy losses observable. One common technique has been to lower the effective gain of selected sense pads in the readout plane. This can be done by lowering the gain of the readout electronics in that channel or by changing the gas amplification at the readout plane. In the EOS TPC [4] this was done by decreasing the voltages in select anode wires in the multi-wire readout. With the prototype Active Target Time Projection Chamber lowering or increasing the gain was achieved by decreasing or increasing the electric fields on selected pads within a Micromegas [3]. The results of changing the gas-gain vs. the electronic gain are rather similar; reducing the gain to obtain the dynamic range indicated by the dashed-dotted magenta lines, making the TPC effectively blind to minimum ionizing particles in the regions of lower gain.

While future developments in TPC electronics may ultimately provide means to significantly improve the dynamic range of TPC electronics, it is useful to

consider whether software strategies can be developed that can compensate for these dynamic range limitations of existing devices. In this paper, we illustrate one approach to expand the dynamic range within the context of a standard  
 65 multi-wire TPC, without the need of extra hardware or dedicating regions of lower gain.

1.1 TPC Overview. We begin our discussion by describing some basic properties of the SAMURAI Pion Reconstruction and Ion-Tracker ( $S\pi$ RIT) TPC [1]. It is a rectangular TPC with 12,096 pads designed to constrain the density dependence  
 70 of the nuclear symmetry energy at densities on the order of twice saturation density. In order to study central collisions of Sn isotopes at 270 AMeV, the TPC was designed to identify isotopes from  $Z=1-3$  with the ability to detect low ionizing particles such as pions.

For ease of illustration and discussion in this paper, we use a coordinate  
 75 systems for the  $S\pi$ RIT TPC, that has the beam traveling along the +z direction. The negative y-axis points away from the pad plane into the drift volume. The positive x-axis pointing to the left of the beam and runs parallel to the wires.

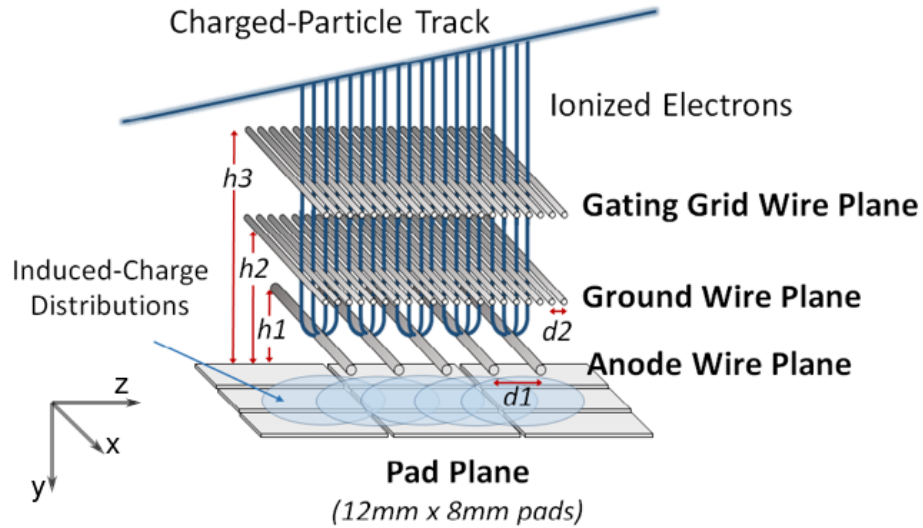


Figure 2: Cartoon graphic showing the 3 wire planes and a section of the pad plane.  $h3 = 14$  mm,  $h2 = 8$  mm,  $h1 = 4$  mm,  $d2 = 1$  mm,  $d1 = 4$  mm.

*Pad plane.* The S $\pi$ RIT TPC pad plane is composed of a rectangular charge sensitive pads, each with an x dimension of 8 mm wide, and a z dimension of 12 mm. These pads are arranged in a grid measuring 112 by 108 pads with a total area of 1344 mm x 864 mm.

*Wire planes.* As illustrated in Figure 2, the S $\pi$ RIT TPC consists of three wire planes below the pad plane, with the wires aligned along the x-axis. The wire plane farthest from the pad plane (14 mm) operates as an ion-gate or a gating grid. Details on the gating grid can be found in [5]. The middle wire plane (8 mm) is grounded. When the gating grid is open, electrons ionized by reaction products in the drift volume drift through both the gating grid and ground planes.

Closest to the pad plane is the high voltage, anode wire plane (4 mm), consisting of 20  $\mu$ m diameter wires spaced 4 mm apart. In the vicinity of these wires an avalanche occurs multiplying the secondary electrons drifting up from the drift volume, created from the track's energy loss in the detector gas. When these secondary electrons reach the anode wires, they are amplified on the order of 1000 times creating electron and ion pairs. It is the motion of these slow moving ions, as they drift away from the anode wires, that induces image charges on the read out pads above. The distribution of image charged on the pad plane is centered about the avalanche region on the wires and its width is fixed by the distance from the pad plane.

The anode wires are sectioned off into 14 independent sections, each containing 26 wires; 12 sections were biased to 1460 V. This setting was optimized to ensure m.i.p. particles such as pions would have a signal to noise ratio of around 20:1. The two remaining sections were biased to 1214 V due to high current issues, reducing the gas gain by a factor of 10 times as compared to the other anode sections. As demonstrated by the EOS TPC [4], lowering the anode wires effectively extended the dynamic range. This gain reduction allowed for a direct validation of the success of the new method for extending the dynamic range presented here.

*Generic Electronics for TPCs.* Signals in the S $\pi$ RIT TPC are amplified and digitized by the recently developed Generic Electronics for TPCs (GET) [6].

110 Short cables transmit the signals from the pads to the inputs of the AGET chips. Each AGET chip services 64 pads (63 pads are connected in our case), contains a pre-amplifier, and a Switched Capacitor Array (SCA), with a maximum of 512 time buckets with an adjustable sampling frequency of 1 to 100 MHz. Four AGET chips are mounted on one AsAd (ASIC and ADC) motherboard. The 115 gain of each AGET can be configured as 0.12, 0.24, 1.0, or 10 pC over the whole dynamic range, and the ADCs on each AsAd board provides 12 bit resolution. The peaking times of the shaping amplifiers can be set to 69, 117, 232, 501, 720, or 1014 ns. In this experiment, the gain was set to the highest setting, 0.12 pC, the peaking time 117 ns, and the sampling frequency 25 MHz (resulting in 40 120 ns time buckets). The AGET 2.0, ASAD 2.1, and COBO 1.0 firmware versions were used. The variations in the electronics were calibrated by measuring the response of each channel to an injected reference pulse, covering the full dynamic range of each channel.

*Analysis Software.* The S $\pi$ RITROOT software is modular task based code 125 based on the FAIRROOT package written in C++ [7]. The S $\pi$ RITROOT reconstruction software is constructed from several main tasks: Decoder task, Pulse Shape Algorithm (PSA), Helix Track Finding Algorithm, Clustering Algorithm, Track Fitting, and Vertex Fitting.

The decoder task converts the binary data file into a container class which 130 maps the electronics channels into the corresponding pads and (x,z) coordinates.

There may be several pulses in a pad coming from two tracks passing under the same pad separated by arrival time. Using an expected pulse shape the PSA task fits the signal pulses within a pad, giving the arrival time of the drifted electrons from each particular track. The height of the fitted pulse 135 is proportional to the total charge of that event, Q and the y-coordinate is calculated as  $y = v \cdot t_0$  where  $v$  is the drift velocity and  $t_0$  the arrival time. Combining the information from these first two tasks, (x,y,z,Q), we construct

what is called a "hit".

The Helix Track Finding Algorithm finds the collection of hits belonging to  
140 one track out of all the hits in an event. The hits within a track are then reduced into clusters. A cluster's position is the average position of the hits within a cluster, with the total charge of the cluster being the sum of the hits charges.

A tracks average position is estimated by the cluster's average position. The clusters are then fitted in the GENFIT track fitting package [8], giving the final  
145 momentum of the track. A final vertex of the event is fitted from all tracks using the package RAVE [9].

*Definition of clustering.* A brief description of the method of clustering is illustrated in Figure 4. It is impractical to cluster in both the x and z-axis and we  
150 only cluster the hits along one axis. The three clusters at the bottom of Figure 4 are clustered along the x-axis and the upper three are along the z-axis, as shown by the bolded pads for one of the clusters in each direction.

The clustering direction depends on the angle of the track with respects to the x-axis, defined as  $\theta$ . For example, a track going along the z-axis the crossing angle is defined as  $90^\circ$ , and a track going along the x-axis defined as  $0^\circ$ . In the  
155 case that the crossing angle is  $45^\circ < \theta \leq 90^\circ$  the clustering direction is along the x-axis. For  $0^\circ < \theta \leq 45^\circ$  it is along the z-axis.

The position along the clustering direction is calculated by weighting the individual hit's positions by their charges  $q_i$  and getting the mean value. The other direction is set to the center of the pad. For example if we are clustering  
160 along the x-axis for a cluster, the z-position is set to the center of the pad in the z-direction and vice versa.

Clustering in this way gives us better position resolution for calculating the position of each cluster. You could imagine if we calculated the clusters only along the x-axis for tracks with  $\theta \approx 0^\circ$  the x-position is not well defined. By  
165 clustering in the direction most perpendicular to the track, we get a better position resolution.

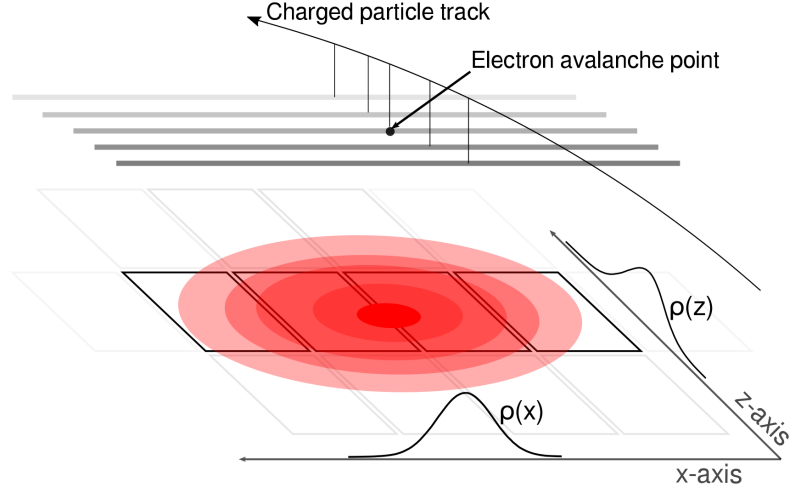


Figure 3: A cartoon illustration of the charge distribution resulting from an electron avalanche on one wire and the projections of the distribution onto the two axis  $\rho(x)$  onto the x-axis and  $\rho(z)$  onto the z-axis. The orientation of the wire planes is flipped upside down to display the perspective better.

## 2. Pad Response Function

As illustrated in Figure 3 the distribution resulting from an electron avalanche is 2-dimensional, with the charge observed on each pad being the integral of that distribution over the pad's dimensions; also called the Pad Response Function (PRF). The projection onto the x and z-axis of this distribution is shown as  $\rho(x)$  and  $\rho(z)$ .

In this example the clustering direction would be along the x-axis, as illustrated by the bolded pads. By choosing to clustering only in one direction, we have not included the charge in adjacent pads along the z-axis resulting from the tails of  $\rho(z)$ . Therefore the charge not included in the the bolded pads will be included in adjacent clusters, introducing small correlations in charge between neighboring clusters.

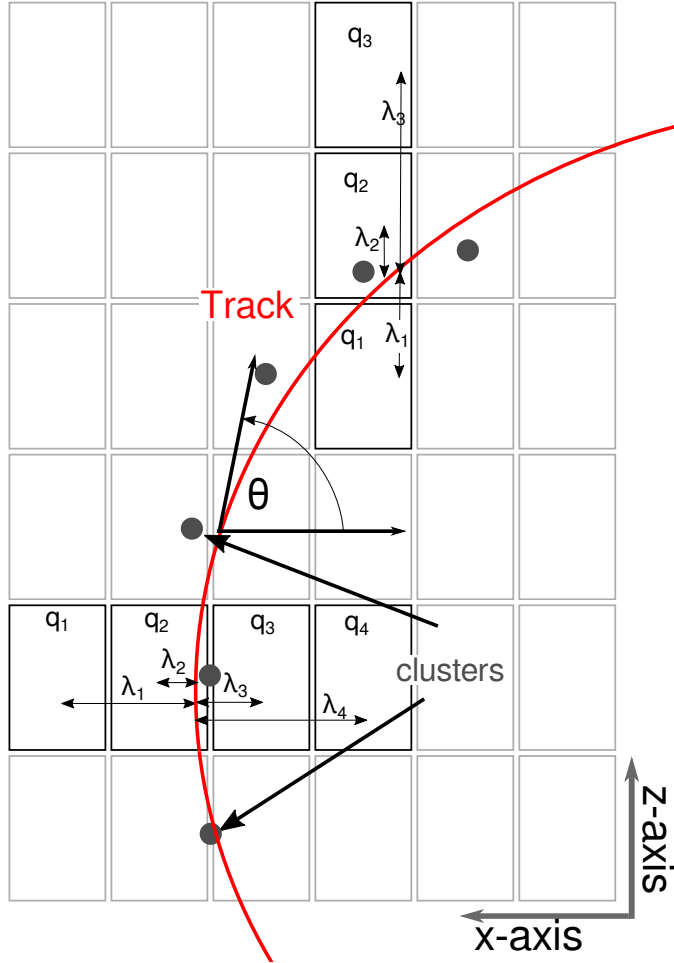


Figure 4: Cartoon graphic of a top down view of a fit to a track passing through several pads. The bolded pads and the charges  $q_i$  represent the hits belonging to that pad and the clusters of the track representing the average position of the track. The three clusters at the bottom are clustered in the x-direction and for the upper three clustered in the z-direction. The estimate of the position of the avalanche is given by the track fit and the position from the center to each pad to the  $\bar{x}$  position is given as  $\lambda_i$ .

**Gatti Pad Response Function.** Gatti [10] expressed a semi-empirical equation for the charge distribution in a simple multi-wire TPC such as that found in the S $\pi$ RIT TPC. Given in Eq. 1, the function depends only on the width of a pad

(w), height of the anode plane to the pad plane (h), and the distance of the pad center to the avalanche point  $\lambda$ . It is a single parameter equation where the two parameters  $K_1 = \frac{K_2\sqrt{K_3}}{4\pi\text{atan}(\sqrt{K_3})}$  and  $K_2 = \frac{\pi}{2} \left(1 - \frac{\sqrt{K_3}}{2}\right)$  depend on the parameter  $K_3$ , which is a function of the ratio of the anode wire diameter to the height of the anode wires to the pad plane.  $K_3$  can be looked up in a graph in [11] and [10].

$$\begin{aligned} PRF_{gatti}(\lambda) &= \frac{K_1}{K_2\sqrt{K_3}} [\arctan(\sqrt{K_3}\tanh[K_2(\frac{\lambda}{h} + \frac{w}{2h})]) \\ &\quad - \arctan(\sqrt{K_3}\tanh[K_2(\frac{\lambda}{h} - \frac{w}{2h})])] \end{aligned} \quad (1)$$

*Experimental PRF.* The correlations we introduced by only clustering along one direction do not play a significant role in the particle identification, but cause deviations from the expected Gatti distribution. Also, analytic PRFs only exist for classical multi-wire TPCs. For these reasons it is useful to experimentally measure the PRF and fit it with some empirical function, typically a Gaussian, to describe its behavior.

As shown in Figure 4, we postulate that the PRF is a function of the total charge deposited in a cluster  $Q = \sum_i q_i$  and the difference in position of the center of the  $i^{th}$  pad,  $x_i$ , to the mean position  $\bar{x} = \sum_i x_i q_i / Q$ , which we call  $\lambda_i = x_i - \bar{x}$ . The PRF is simply defined as the charge fraction of each pad as a function of  $\lambda$ , Equation 2.

$$PRF(\lambda_i) = \frac{q_i(\lambda_i)}{Q} \quad (2)$$

Averaging over many events in the experimental data, the resulting PRF for the S $\pi$ RIT TPC is shown in Figure 5. Here we see the deviations from the expected analytic Gatti distribution where as fitting with a two parameter Gaussian function describes the data better. With the two parameters being the normal coefficient,  $N_0$ , sigma  $\sigma$ , and with a mean value assumed to be 0 as given in Equation 3.

$$PRF_{gaus}(\lambda) = N_0 e^{\frac{-\lambda^2}{2\sigma^2}} \quad (3)$$

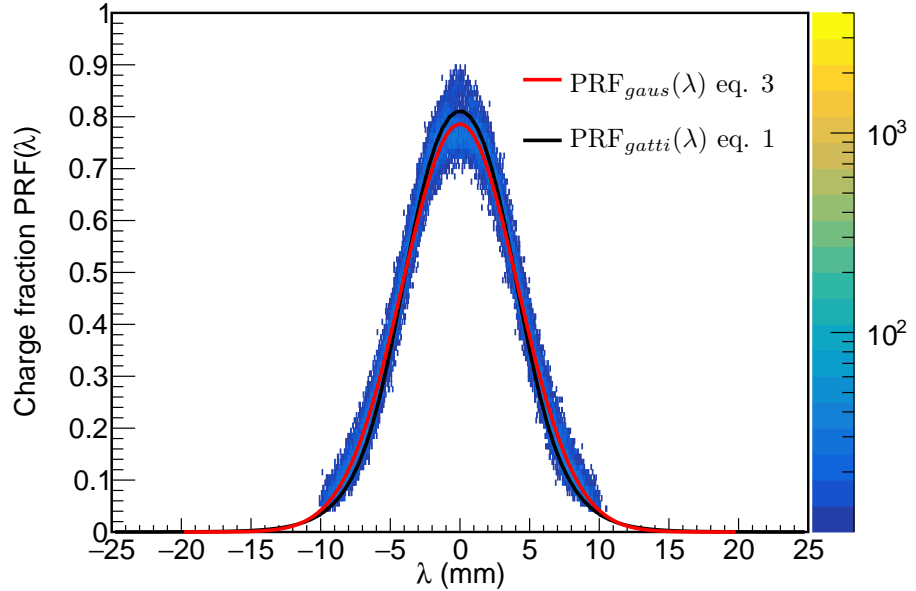


Figure 5: Experimental pad response function of many events for a crossing angle of  $85^\circ < \theta \leq 90^\circ$ .

### 205 3. PRF vs crossing angle

The shape of the PRF depends on the crossing angle [10]. As plotted in Figure 6 is the PRF of a  $\pi^-$  tracks vs the crossing angle  $\theta$ . One can see the PRF gets wider going from  $90^\circ$  to  $45^\circ$ . Once could imagine if we did not switch clustering directions the PRF would become wider until it was a uniform distribution and there was no position resolution. Since we switch the clustering direction from x to z at  $45^\circ$ , the opposite trend is seen where the PRF becomes narrower going from  $45^\circ$  to  $0^\circ$ .

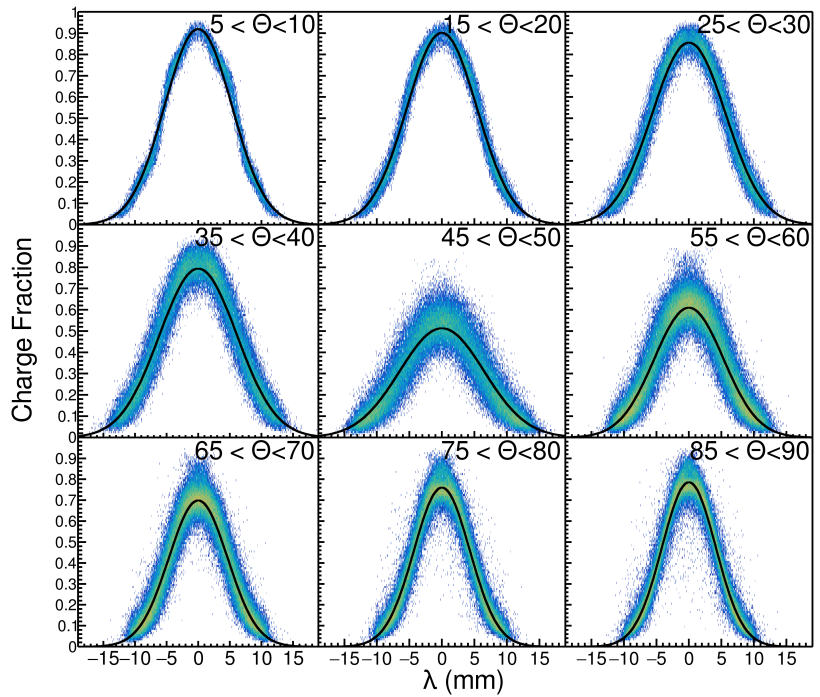


Figure 6: Experimental pad response function as a function of the crossing angle  $\theta$

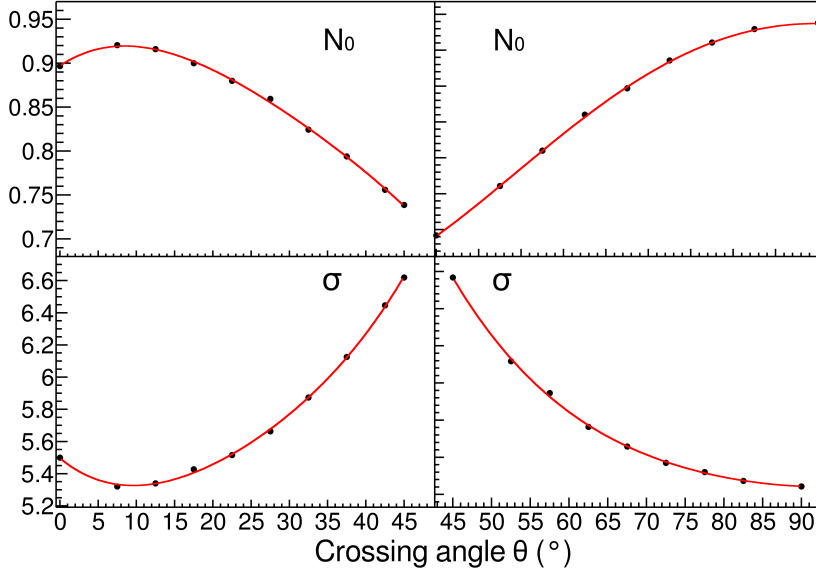


Figure 7: Parameters  $N_0$  and  $\sigma$  as a function of the crossing angle  $\theta$  with the 4<sup>th</sup> order polynomial fits.

Fit's were performed to the experimental data with  $5^{\circ}$  width bins from  $0^{\circ} < \theta \leq 90^{\circ}$ . The two parameters of the Gaussian fits are plotted versus  $\theta$  in Figure 7; a 4<sup>th</sup> order polynomial fit between these points allowed for interpolating between  $\theta$ .

*Method of Desaturation.* We will use the term "desaturation" for our process of correcting the charge values of the saturated pads. Figure 8 shows a typical situation of saturated signals. When an avalanche causes a large induced signal, the pads directly underneath collect the largest charge becoming saturated represented by  $q_2$  and  $q_3$ . Pads further away experience smaller, non saturating charges represented by  $q_1$  and  $q_4$ . Though we don't know the saturated charge values, the distribution of all charges must follow the PRF which we have experimentally measured. From the clusters crossing angle, we can get the corresponding parameters for the PRF as described above in Figure 7.

We assume the distance of each pad to the track,  $\lambda_i$  is fixed, this defines the

fraction of charge each pad receives as defined by the  $PRF(\lambda_i)$  function.

A chi squared function,  $\chi^2 = \sum_i \frac{(q_i^{obs} - q_i^{expect})^2}{q_i^{expect}}$ , where  $q_i^{obs}$  are the observed, non-saturated charges  $q_1$  and  $q_4$ , and  $q_i^{expect}$  are the expected charges observed; calculated as  $q_i^{expected} = Q \cdot PRF(\lambda_i)$ . The charges,  $q_{2'}$ ,  $q_{3'}$ , make up the unknown variable and are allowed to vary in the  $\chi^2$  minimization but are added to make up the total expected charge  $Q$ . The minimum of the  $\chi^2$  distribution gives best estimate for the saturated charge values on each pad.

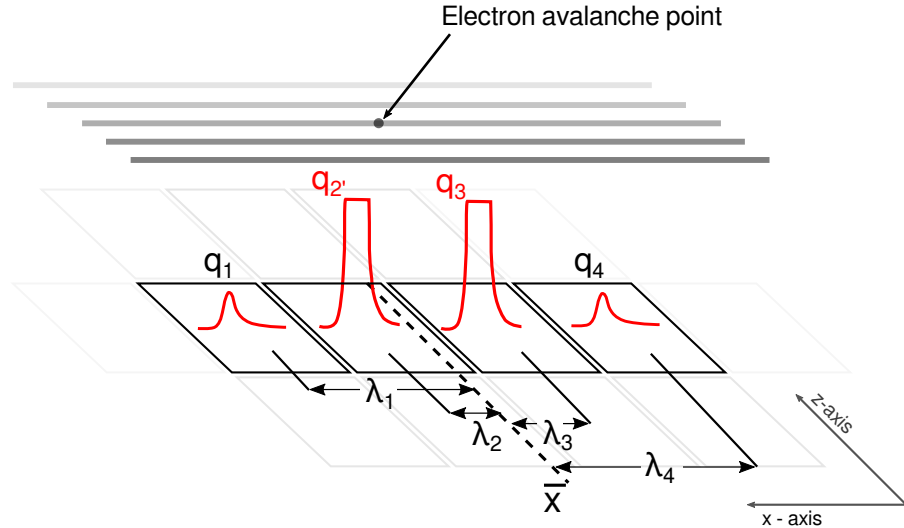


Figure 8: A typical case of a saturating event. The red pulses represent the time bucket signal for each collected charge. The pads directly underneath the avalanche point,  $q_{2'}$  and  $q_{3'}$ , are saturated while pads farther away,  $q_1$  and  $q_4$  are not saturated.

#### 4. Experimental data

Two sets of data were used for the testing and validation of this method. A cocktail beam consisting of ( $p, d, t, {}^3He, {}^4He, {}^6Li, {}^7Li$ ) light charged particles was injected into the TPC for calibration purposes, and tuned to two different rigidity,  $\beta\rho$ , settings. The momentum resolution was approximately 1%, as determined by the slits of the BigRIPS fragment separator of the Radioactive Isotope Beam Factory (RIBF) in RIKEN. A thick 21 mm thick aluminum target

was inserted for part of the lower  $\beta\rho$  setting, further reducing the energy of the beam for a third calibration point.

In a typical cocktail event, one particle enters the TPC volume at a time and parallel to the pad plane, representing an ideal case for momentum and  $dE/dx$  determination; as it does not suffer from inefficiencies of high multiplicity events seen in the collision experimental data.  
245

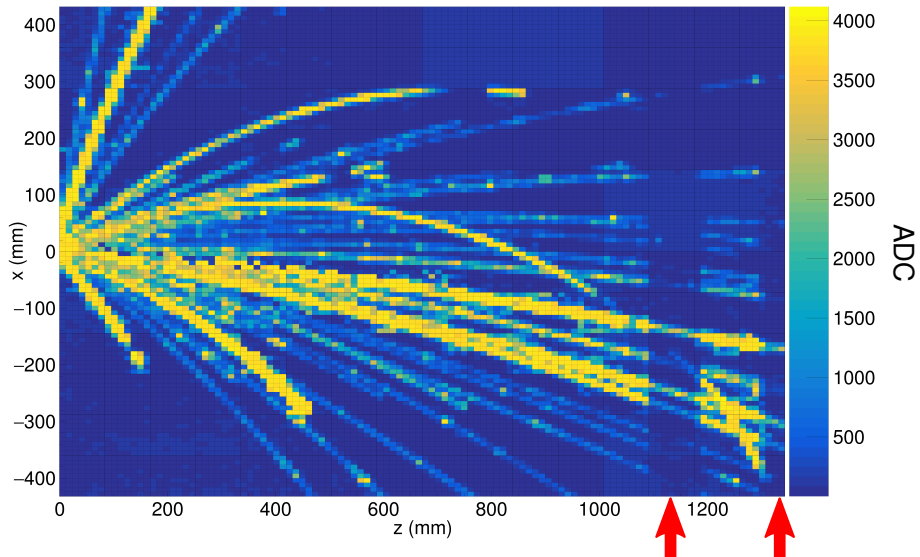


Figure 9: Pad plane projection for a collision event in the TPC. Highlighted by red arrows are two regions of anode wires which had a reduced voltage of 1214 V. The voltage of the rest of the TPC anode wires are 1460 V. The reduction in voltage reduces the gain by a factor of about 10x.

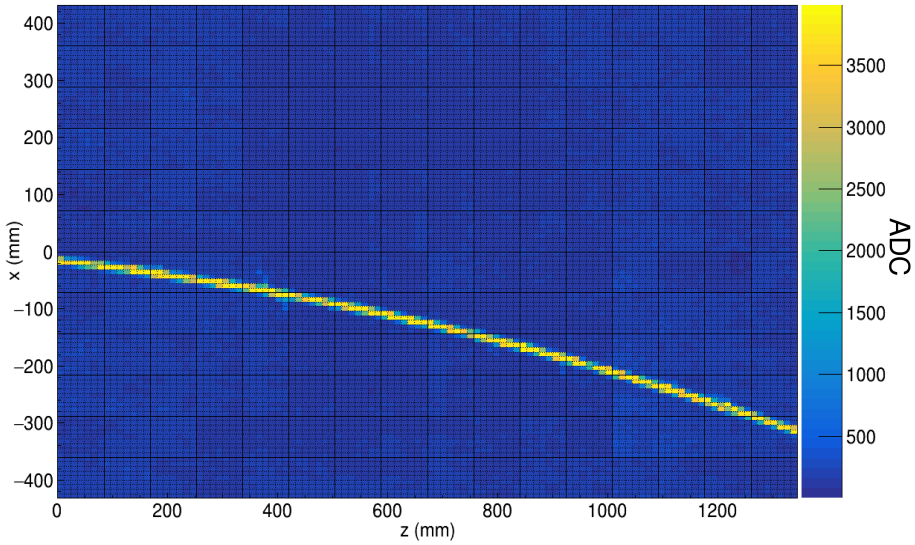


Figure 10: Pad plane projection for a cocktail event in the TPC.

The other type of data was the collision of a  $^{132}\text{Sn}$  beam onto a  $^{124}\text{Sn}$  target triggered on central nuclear collisions. Shown in Figure 9 is the typical pad plane response for a central nuclear collision. During the experiment the voltages of two anode sections (as indicated by red arrows in Figure 9) were biased to 1214 V. The gain of these sections were also reduced by a factor of about 10 times, as compared with the other sections which were biased to 1460 V. We refer to the 1460 V region as high gain and the 1214 V region as low gain.  
250

## 5. Results

255 *Low gain vs corrected high gain.* Tracks which saturate pads in the high gain region are not saturated in the low gain region; by comparing the  $dE/dx$  values of these two sections, we can directly measure the success of the high gain region's desaturation using the method described above.

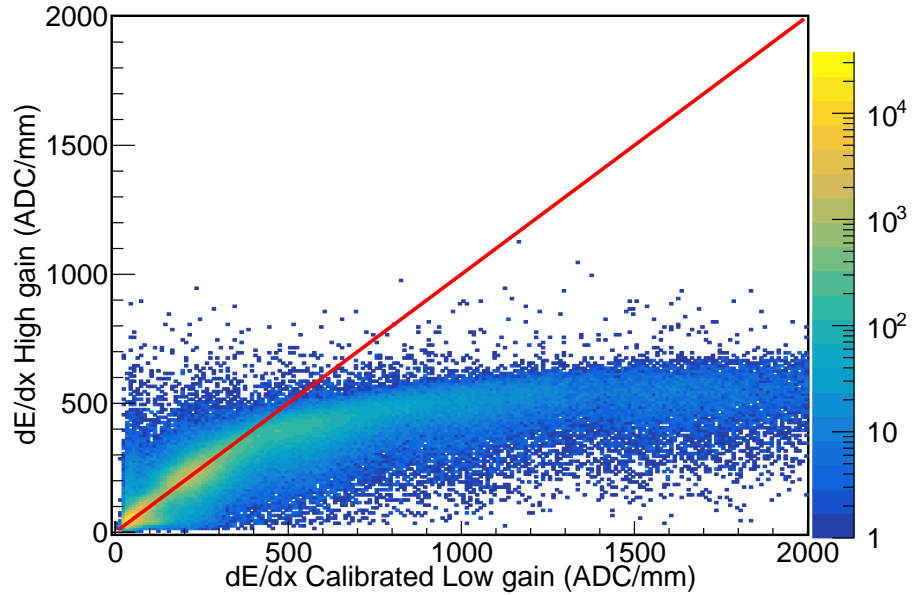


Figure 11: The uncorrected high gain  $dE/dx$  vs low gain  $dE/dx$  collision data.

In Figure 11, the effect of saturation can be seen in the high gain region for  
 260 the uncorrected data. For signals below 400 ADC/mm the electronics are not  
 saturated, and therefore the high and low gain sections agree. The data starts  
 to saturate above 400 ADC/mm in the high gain channels eventually reaching a  
 plateau; the low gain sections have not saturated and provide true  $dE/dx$  values.  
 After applying the desaturation method, the correlation between the high and  
 265 low gain sections is restored, as seen in Figure 12. We believe the correction to  
 at least about 2000 ADC/mm, increasing the dynamic range by a factor of 5.

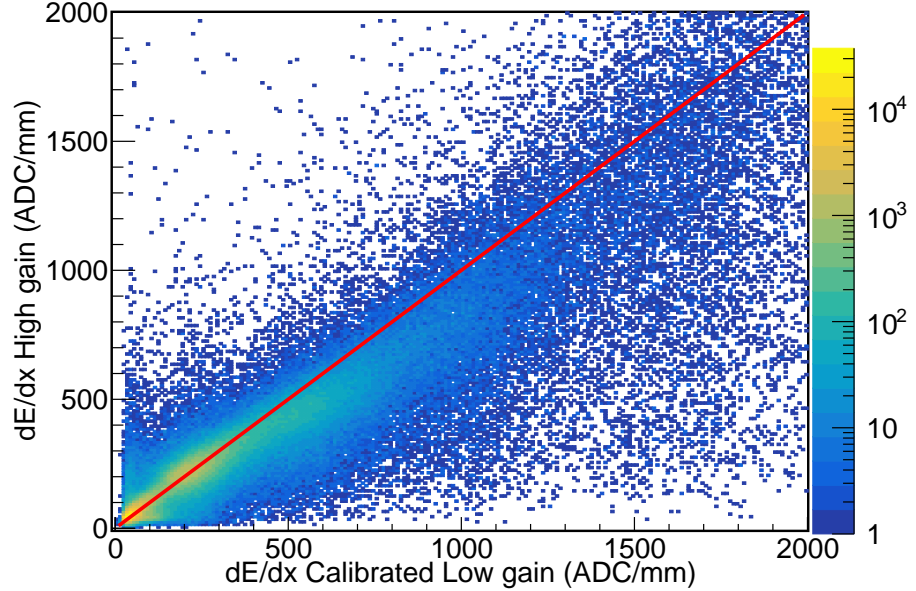


Figure 12: The corrected high gain  $dE/dx$  vs low gain  $dE/dx$  for collision data.

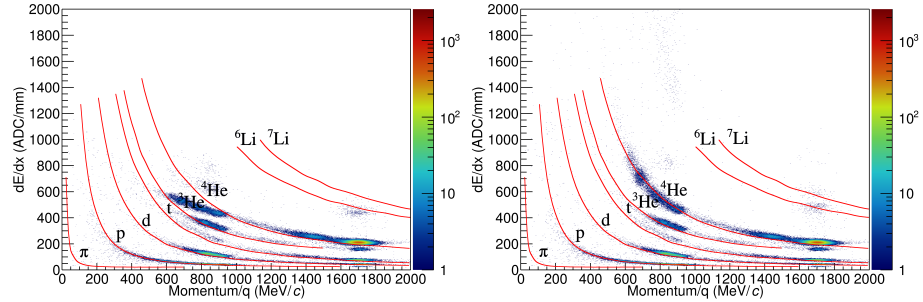


Figure 13: Uncorrected and corrected (desaturated) cocktail data.

*Particle Identification (PID).* Comparing the low to high gain sections provides a direct measurement for determining the success of the desaturation technique, but the goal would be to improve the particle identification (PID). In the following PID plots the red lines represent the most probable energy loss as given by Geant4 straggling functions. A linear calibration was performed to convert keV in Geant4 to ADC in the experiment given by  $\frac{ADC}{mm} = 20 \cdot \frac{keV}{cm}$ .

There are pronounced PID lines of several particle species in both the uncorrected and corrected cocktail beam PID in figures 13. Three ovals around  
275 a momentum of 1700 and two near 900 MeV/c/Z correspond to the three  $B\rho$  settings injected into the TPC. The tails of the PID lines resulting from the particle losing its initial energy, passing through the walls and other materials outside the main detector volume; therefore lowering their initial momentum.

The uncorrected data in Figure 13 shows the effects of saturation; the PID  
280 lines deviate from their theoretical expectations starting around 400 ADC/mm eventually reaching a plateau. After applying the desaturation technique, we see a large improvement; most notably the He and Li particles, which suffer the most from saturation. A more subtle improvement of the lighter particles, (p,d,t), can also be seen in the PID lines at lower momentum.

285 Looking at the collision data, in figure ??, we also see a similar result. The collision data PID suffers from more background and inefficiencies than the cocktail beam; nevertheless we can see a similar improvement in the PID lines when comparing the uncorrected to after the desaturation has been applied. Notably the separation of particle species at lower momenta and the separation  
290 of the Li species into  ${}^6\text{Li}$  and  ${}^7\text{Li}$ , whereas there was little to no separation before.

## 6. Conclusion

The saturation of the electronics reduces  $dE/dx$  resolution and even the maximum charge observable inside of a TPC. We have shown that some of  
295 the saturation is recoverable. Since the Pad Response Function of the TPC is fixed by the anode wire geometries, an experimental PRF can be calculated from the unsaturated experimental data. The charge distribution resulting from an avalanche on a wire must follow this PRF even if the electronics of some channels directly under the avalanche are saturated. The pads further away are  
300 not saturated; by using these unsaturated pads we perform applying a  $\chi^2$  fit the unknown saturated pads to the known PRF.

Looking at the PID lines, and also making a direct comparison to some low gain sections of the TPC, we were able to extend the dynamic range of our electronics by a factor of about 5 times. This improved PID will allow for us to  
305 extend the momentum distributions of all species to lower momenta than what was previously available.

## 7. Acknowledgments

This work was supported by the U.S. Department of Energy under Grant Nos. DE-SC0004835, DE-SC0014530, DE-NA0002923, US National Science  
310 Foundation Grant No. PHY-1565546, the Japanese MEXT KAKENHI(Grant-in-Aid for Scientific Research on Innovative Areas) grant No. 24105004, and Polish National Science Center (NCN), under contract Nos. UMO-2013/09/B/ST2/04064 and UMO-2013/10/M/ST2/00624. The computing resources for analyzing the data was provided by the HOKUSAI-GreatWave system at RIKEN and the  
315 MSU HPCC.

## References

- [1] R. S. et. al., S $\pi$ rit: A time-projection chamber for symmetry-energy studies, NIM A 784 (2015) 513–517. doi:[10.1016/j.nima.2015.01.026](https://doi.org/10.1016/j.nima.2015.01.026).
- [2] H. Bichsel, A method to improve tracking and particle identification in tpc  
320 and silicon detectors, Nucl. Instr. Meth. Phys. Res. A 562 (2006) 154–197.  
doi:[10.1016/j.nima.2006.03.009](https://doi.org/10.1016/j.nima.2006.03.009).
- [3] D. S. et. al., Prototype at-tpc: Toward a new generation active target time projection chamber for radioactive beam experiments, Nucl. Instr. Meth. Phys. Res. A 691 (1) (2012) 39–58. doi:[10.1016/j.nima.2012.06.050](https://doi.org/10.1016/j.nima.2012.06.050).
- [4] G. R. et. al., A tpc detector for the study of high multiplicity heavy ion  
325 collisions, IEEE Transactions on Nuclear Science 37 (2) (1990) 56–64. doi:[10.1109/23.106592](https://doi.org/10.1109/23.106592).

- [5] S. et. al., A gating grid driver for time projection chambers, Nucl. Instr. Meth. Phys. Res. A 853 (2017) 44–52. doi:[10.1016/j.nima.2017.02.001](https://doi.org/10.1016/j.nima.2017.02.001).
- 330** [6] E. P. et. al., Get: A generic and comprehensive electronics system for nuclear physics experiments, Physics Procedia 37 (2012) 1799–1804. doi:[10.1016/j.phpro.2012.02.506](https://doi.org/10.1016/j.phpro.2012.02.506).
- [7] M. A.-T. et. al., The fairroot framework, J. Phys.: Conf. Ser. 396 (2). doi:[10.1088/1742-6596/396/2/022001](https://doi.org/10.1088/1742-6596/396/2/022001).
- 335** [8] C. H. et. al., A novel generic framework for track fitting in complex detector systems, Nucl. Instrum. Meth. A 620 (2-3) (2010) 518–525. doi:[10.1016/j.nima.2010.03.136](https://doi.org/10.1016/j.nima.2010.03.136).
- [9] W. Waltenberger, RaveâĂTa detector-independent toolkit to reconstruct vertices, IEEE Transactions on Nuclear Science 58 (2) (2011) 434–444. doi:[10.1109/TNS.2011.2119492](https://doi.org/10.1109/TNS.2011.2119492).
- 340** [10] E. G. et. al., Optimum geometry for strip cathodes or grids in mwpc for avalanche localization along the anode wires, Nucl. Instr. Meth. Phys. Res. A 163 (1979) 83–92. doi:[10.1016/0029-554X\(79\)90035-1](https://doi.org/10.1016/0029-554X(79)90035-1).
- [11] W. Blum, W. Riegler, L. Rolandi, Particle Detection with Drift Chambers, Springer, Berlin, Heidelberg, 2008.
- 345**